

FOURTH-ORDER PARTIAL DIFFERENTIAL EQUATIONS FOR EFFECTIVE IMAGE DENOISING

SEONGJAI KIM, HYEONA LIM

ABSTRACT. This article concerns mathematical image denoising methods incorporating fourth-order partial differential equations (PDEs). We introduce and analyze *piecewise planarity conditions* (PPCs) with which unconstrained fourth-order variational models in continuum converge to a piecewise planar image. It has been observed that fourth-order variational models holding PPCs can restore better images than models without PPCs and second-order models. Numerical schemes are presented in detail and various examples in image denoising are provided to verify the claim.

1. INTRODUCTION

During the previous decade or so, mathematical frameworks employing powerful tools of partial differential equations (PDEs) and functional analysis have emerged and successfully applied to various image processing (IP) tasks, particularly for image restoration [1, 3, 4, 8, 11, 13, 17, 18, 21]; see also [2, 5]. Those PDE-based models have allowed researchers and practitioners not only to introduce effective models but also to improve traditional algorithms in image denoising. However, these PDE-based models tend to either converge to a piecewise constant image or introduce image blur (undesired dissipation), partially because the models are derived by minimizing a functional of the image gradient. As a consequence, the conventional PDE-based models may lose interesting fine structures during the denoising. In order to reduce the artifact, researchers have studied various mathematical and numerical techniques which either incorporate diffusion modulation, constraint terms, and iterative refinement [9, 11, 12, 14] or minimize a functional of second derivatives of the image [10, 16, 20]. These new mathematical models may preserve fine structures better than conventional ones; however, more advanced models and appropriate numerical procedures are yet to be developed.

In this article, we will introduce and analyze *piecewise planarity conditions* (PPCs) with which unconstrained fourth-order variational models in continuum converge to a piecewise planar image. Although such a mathematical theory may not hold for discrete data (images) in the same way as in continuum, it will provide

2000 *Mathematics Subject Classification.* 35K55, 65M06, 65M12.

Key words and phrases. Variational approach; PDE-based restoration model; fourth-order PDEs; piecewise planarity condition.

©2009 Texas State University - San Marcos.

Published April 15, 2009.

a mathematical background for the advancement of the state-of-the-art methods for PDE-based image denoising. It has been observed that fourth-order variational models holding the PPCs can restore images better than second-order models and other fourth-order ones. Fourth-order models have proved to restore texture regions favorably, while second-order models tend to restore edges of large contrasts more clearly.

In the next section, we briefly review variational approaches for second-order and fourth-order PDE-based models in image denoising. Section 3 considers the PPCs for fourth-order variational models. In Section 4, we present difference schemes for fourth-order models, a variable constraint parameter, and a timestep size for a stable simulation. Section 5 contains numerical experiments along with comparisons among various fourth-order models and a second-order model. Our development and experiments are concluded in Section 5.

2. PRELIMINARIES

This section reviews briefly variational approaches for second-order and fourth-order PDE-based models.

2.1. Second-order PDEs. Let the observed image (u_0) be given as

$$u_0 = u + v,$$

where u is the desired image and v denotes a Gaussian noise of mean zero. Then, second-order denoising models [8, 9, 12, 17, 18] can be obtained by minimizing an energy functional of the image gradient,

$$u = \arg \min_u \left[\int_{\Omega} \rho(|\nabla u|) d\mathbf{x} + \frac{\lambda}{2} \int_{\Omega} (u_0 - u)^2 d\mathbf{x} \right], \quad (2.1)$$

where Ω is the image domain, $\lambda \geq 0$ denotes the constraint parameter, and ρ is a function having the properties:

$$\rho(s) \geq 0, \quad s \geq 0; \quad \rho'(s) > 0, \quad s > 0. \quad (2.2)$$

In this article, we will call ρ a *modulator*.

It is often convenient to transform the minimization problem (2.1) into a differential equation, called the *Euler-Lagrange equation*, by applying the variational calculus [19] and parameterizing the energy descent direction by an artificial time t :

$$\frac{\partial u}{\partial t} = \nabla \cdot \left(\rho'(|\nabla u|) \frac{\nabla u}{|\nabla u|} \right) + \lambda (u_0 - u). \quad (2.3)$$

For example, the model (2.3) is reduced to the *total variation* (TV) model [18] for $\rho(s) = s$ and the *Perona-Malik* (PM) model [17] when $\rho(s) = \frac{1}{2}K^2 \ln(1 + s^2/K^2)$, for some $K > 0$, and $\lambda = 0$. For the PM model, the modulator ρ is strictly convex for $s < K$ and strictly concave for $s > K$. (K is a threshold.) Thus the model can enhance image content having large gradient magnitudes such as edges; however, it will flatten slow transitions. For a later frequent use, we define

$$\rho_{PM}(s) := \frac{K^2}{2} \ln \left(1 + \frac{s^2}{K^2} \right), \quad K > 0. \quad (2.4)$$

Most of conventional variational restoration models have a tendency to converge to a piecewise constant image. Such a phenomenon is called the *staircasing effect*.

Although these results are important for understanding of the current diffusion-like models, the resultant signals may not be desired in applications where the preservation of both slow transitions and fine structures is important. In order to suppress the staircasing effect and improve the restorability of second-order PDE models, variants have been suggested incorporating diffusion modulation, different constraint terms, and iterative refinement [9, 11, 12, 14]; see also [21]. For example, for an effective suppression of staircasing, Marquina-Osher [11] have suggested to scale the stationary part of the TV model by $|\nabla u|$:

$$\frac{\partial u}{\partial t} = |\nabla u| \nabla \cdot \left(\frac{\nabla u}{|\nabla u|} \right) + \lambda |\nabla u| (u_0 - u), \quad (2.5)$$

which is called the *improved total variation* (ITV) model [15].

2.2. Fourth-order PDEs. An approach which derives a fourth-order PDE is to minimize an energy functional of the image Laplacian [20]:

$$u = \arg \min_u \int_{\Omega} \rho(|\Delta u|) \, d\mathbf{x}, \quad (2.6)$$

where Δ denotes the Laplacian operator. It is not difficult to check that the associated Euler-Lagrange equation reads

$$\frac{\partial u}{\partial t} = -\Delta \left(\rho'(|\Delta u|) \frac{\Delta u}{|\Delta u|} \right). \quad (2.7)$$

As in You-Kaveh [20], one can prove that when the modulator $\rho = \rho_{PM}$, the solution of (2.7) converges to a piecewise harmonic image, i.e., $\Delta u \rightarrow 0$ locally, as $t \rightarrow \infty$. (Although the authors used the term “piecewise planar”, it must be understood as “piecewise harmonic”.)

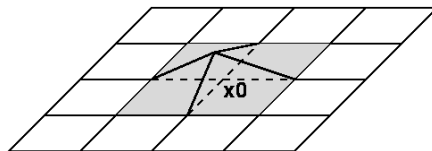


FIGURE 1. A locally smooth surface on the domain of (4×4) subdomains. Let the height on boundary subdomains be zero for simplicity. A locally harmonic surface can be defined on the whole domain for an arbitrary height at \mathbf{x}_0 .

The You-Kaveh model [20] often introduces speckles in an objectionable level. The authors claimed it was due to a less *masking capability* of (2.7) than second-order models. However, the local harmonicity is not sufficient for an effective denoising. To see this, we consider a simple cartoon image as in Figure 1, where a locally harmonic surface can be formed on the image domain for an arbitrary value at the point \mathbf{x}_0 . Thus, for a given perturbation (due to noise), the You-Kaveh model can result in a locally harmonic surface possibly keeping the noise perturbation, instead of suppressing it. This is why the You-Kaveh model tends to introduce speckles, as shown in Figure 6 below.

Other approaches incorporating fourth-order PDEs can be found in [10]:

$$u = \arg \min_u \left\{ \int_{\Omega} |\mathcal{D}u| \, d\mathbf{x} + \frac{\lambda}{2} \int_{\Omega} (u_0 - u)^2 \, d\mathbf{x} \right\}, \quad (2.8)$$

where $\lambda \geq 0$ denotes a constraint parameter and

$$|\mathcal{D}u| = \begin{cases} |\Sigma u| := |u_{xx}| + |u_{yy}|, & \text{or} \\ |\Theta u| := (u_{xx}^2 + u_{xy}^2 + u_{yx}^2 + u_{yy}^2)^{1/2}. \end{cases}$$

The corresponding Euler-Lagrange equations read respectively

$$\begin{aligned} \frac{\partial u}{\partial t} &= -\left(\frac{u_{xx}}{|u_{xx}|}\right)_{xx} - \left(\frac{u_{yy}}{|u_{yy}|}\right)_{yy} + \lambda(u_0 - u), \\ \frac{\partial u}{\partial t} &= -\left(\frac{u_{xx}}{|\Theta u|}\right)_{xx} - \left(\frac{u_{xy}}{|\Theta u|}\right)_{yx} - \left(\frac{u_{yx}}{|\Theta u|}\right)_{xy} - \left(\frac{u_{yy}}{|\Theta u|}\right)_{yy} + \lambda(u_0 - u). \end{aligned} \quad (2.9)$$

These fourth-order PDE-based models have proved to be superior to (2.7) for an appropriate choice of λ . Note that the functional in (2.8) is convex ($\rho(s) = s$). Thus, when $\lambda = 0$, the minimization will converge to a *globally* planar image.

In this article, we will first find conditions for which non-constrained fourth-order PDE-based restoration models converge to a *piecewise* planar image. Then, a comparison study will be performed for various differential operators (\mathcal{D}) and modulators (ρ). Properties of a variational model are combined effects of the differential operator, the modulator, and the constraint term.

3. PIECEWISE PLANARITY CONDITIONS

We first define a vector-valued second-order differential operator

$$\Pi_\zeta = (\partial_{xx}, \zeta \partial_{xy}, \zeta \partial_{yx}, \partial_{yy})^T, \quad \zeta \geq 0, \quad (3.1)$$

where the superscript T denotes the transpose. Since $|\Pi_0 u| \leq |\Sigma u| \leq \sqrt{2} |\Pi_0 u|$, the minimization problem with $|\mathcal{D}u| = |\Sigma u|$ is equivalent to the one with $|\mathcal{D}u| = |\Pi_0 u|$. Thus in this section we will focus on second-order differential operators Π_ζ , $\zeta \geq 0$.

Consider a minimization problem of the form

$$u = \arg \min_u \int_\Omega \rho(|\mathcal{D}u|) \, d\mathbf{x}, \quad \mathcal{D} = \Pi_\zeta, \quad \zeta \geq 0. \quad (3.2)$$

Then, the associated evolutionary Euler-Lagrange equation reads

$$\frac{\partial u}{\partial t} = -\mathcal{D} \cdot \left(\rho'(|\mathcal{D}u|) \frac{\mathcal{D}u}{|\mathcal{D}u|} \right). \quad (3.3)$$

Note that $|\Pi_\zeta u| = 0$, $\zeta > 0$, if and only if the solution u is globally planar. On the other hand, $|\Pi_0 u| = 0$ when u is globally bilinear. Since

$$|\Delta u| \leq \sqrt{2} |\Pi_\zeta u|, \quad \zeta \geq 0, \quad (3.4)$$

it is easy to see that a minimizer of (3.2) is also a minimizer of (2.6). However, the reverse is not true; a minimizer of (2.6) may not be a minimizer of (3.2).

The following theorem proves that for selected modulators ρ , piecewise planar images are the only minimizers of (3.2) (equivalently, the only stationary states of (3.3)), when the restored image is to be continuous and piecewise smooth.

Theorem 3.1. *Suppose that u is continuous and piecewise smooth. Let ρ satisfy (2.2) and*

$$\rho(0) = 0, \quad \lim_{s \rightarrow \infty} \frac{\rho(s)}{s} = 0. \quad (3.5)$$

Then u is piecewise planar if and only if

$$\int_{\Omega} \rho(|\mathcal{D}u|) \, d\mathbf{x} = 0, \quad \mathcal{D} = \Pi_{\zeta}, \quad \zeta > 0. \tag{3.6}$$

Proof. (\Rightarrow) Let u be piecewise planar. Consider the corresponding partition of Ω : $\{\Omega_j\}_{j=1}^M$, for some $M > 0$, on each of which the image is planar. Let us denote the interior and the boundary of Ω_j by Ω_j^0 and $\partial\Omega_j$, respectively. Define $\Gamma_{jk} = \partial\Omega_j \cap \partial\Omega_k$, the edge between neighboring subregions Ω_j and Ω_k . Then, it is easy to see that Γ_{jk} are straight line segments. Let $u_j = u|_{\Omega_j}$. Then, for $\mathcal{D} = \Pi_{\zeta}$, $\zeta > 0$,

$$|\mathcal{D}u_j(\mathbf{x})| \equiv 0, \quad \forall \mathbf{x} \in \Omega_j^0, \quad j = 1, \dots, M. \tag{3.7}$$

On the other hand, ∇u_j are constant vectors on each Ω_j , $j = 1, \dots, M$. Without loss of generality, we may assume that

$$\nabla u_j \neq \nabla u_k, \quad \forall \mathbf{x} \in \Gamma_{jk}, \quad j, k = 1, \dots, M. \tag{3.8}$$

So we have $|\mathcal{D}u(\mathbf{x})| = \infty$, $\forall \mathbf{x} \in \cup_{jk} \Gamma_{jk}$.

In order to deal with the integral of the infinite on a set of measure zero, let $\Omega_{jk}^{\varepsilon}$ be the ε -rectangle of Γ_{jk} that has the same length as Γ_{jk} and a width of ε in a normal direction of Γ_{jk} , with Γ_{jk} being centered. Define $S_{jk}^{(\varepsilon)}$ on $\Omega_{jk}^{\varepsilon}$ to have the property that $\nabla S_{jk}^{(\varepsilon)}$ becomes a linear transition between ∇u_j and ∇u_k . Then, $|\mathcal{D}S_{jk}^{(\varepsilon)}|$ is a constant on $\Omega_{jk}^{\varepsilon}$: $|\mathcal{D}S_{jk}^{(\varepsilon)}| = c_1/\varepsilon$, for some $c_1 > 0$. Thus, by denoting the length of Γ_{jk} by c_{jk} , we have

$$\int_{\Omega_{jk}^{\varepsilon}} \rho(|\mathcal{D}S_{jk}^{(\varepsilon)}|) \, d\mathbf{x} = \rho(c_1/\varepsilon) \cdot c_{jk}\varepsilon. \tag{3.9}$$

It therefore follows from (3.5) and (3.9) that

$$\int_{\Gamma_{jk}} \rho(|\mathcal{D}u|) \, d\mathbf{x} = \lim_{\varepsilon \rightarrow 0} \int_{\Omega_{jk}^{\varepsilon}} \rho(|\mathcal{D}S_{jk}^{(\varepsilon)}|) \, d\mathbf{x} = 0. \tag{3.10}$$

Note that the above holds for all Γ_{jk} , $j, k = 1, \dots, M$; (3.6) follows from (3.7) and (3.10).

(\Leftarrow) Let u be continuous and piecewise smooth and satisfy (3.6). Then, since $\rho(0) = 0$ and $\rho(s) > 0$ for $s > 0$, the quantity $|\mathcal{D}u|$ must be zero at least at all interior points of the subregions in which u is smooth; which implies that u is piecewise planar. This completes the proof. \square

Remarks. From the above theorem we have few remarks:

- The PPCs are (3.5) and $\mathcal{D} = \Pi_{\zeta}$ for $\zeta > 0$. The choice $\mathcal{D} = \Delta$ or $\mathcal{D} = \Pi_0$ is not a part of PPCs. The model with (3.5) and $\mathcal{D} = \Pi_0$ would converge to a piecewise bilinear image.
- The conditions in (3.5) implies that the modulator ρ must be non-convex, at least for large values of s . Non-convex modulators are, for example,

$$\rho(s) = \rho_{\alpha}(s) := \frac{1}{\alpha} s^{\alpha}, \quad 0 < \alpha < 1; \quad \rho(s) = \rho_{PM}(s). \tag{3.11}$$

- Minimizers of (3.6) are not unique; each of all piecewise planar images is a minimizer. Thus it is a good idea to incorporate a constraint term in order for the resulting model to converge to a *desirable* piecewise planar image, closer to the given image, that preserves fine structures satisfactorily.

- The diffusion magnitude $|\mathcal{D}u|$ never approaches the infinity for (bounded) discrete data. Thus the minimization process in (3.2) may not completely avoid a tendency of converging to a *globally* planar image. However, the tendency will be weaker than the convex minimization as in (2.8). By incorporating a proper constraint term, non-convex fourth-order PDEs can restore better images, as numerically verified in Section 5.

4. DIFFERENCE SCHEMES

We rewrite the models in (2.7) and (3.3), incorporating a constraint term, as

$$\frac{\partial u}{\partial t} = -\mathcal{D} \cdot \left(\frac{\mathcal{D}u}{\mathcal{P}(u)} \right) + \lambda(u_0 - u), \quad \mathcal{D} = \Delta, \Pi_\zeta, \zeta \geq 0, \quad (4.1)$$

where

$$\mathcal{P}(u) = \frac{|\mathcal{D}u|}{\rho'(|\mathcal{D}u|)}.$$

Note that one can apply a (linearized) implicit time-stepping scheme to the above model when the nonlinear part $\mathcal{P}(u)$ is evaluated from the previous time level. In that case, the models with $\mathcal{D} = \Pi_0$ are separable such that they can be efficiently simulated by the alternating direction implicit (ADI) method [6, 7, 8]. In this article, for simplicity, we will employ the explicit time-stepping procedure for all models in (4.1).

Let Δt^n be the n th timestep size, $t^n = \sum_{k=0}^{n-1} \Delta t^k$, and $g^n = g(\cdot, t^n)$ for a function of time (and the spatial variables). Given $u_0 = u^0, u^1, \dots, u^n$, the explicit scheme computes u^{n+1} *explicitly* as

$$\begin{aligned} \frac{u^{n+1} - u^n}{\Delta t^n} &= -A_{\mathcal{D}}^n u^n + \lambda^n (u_0 - u^n), \\ A_{\mathcal{D}}^n u^n &:= \mathcal{D}_h \cdot \left(\frac{\mathcal{D}_h u^n}{\mathcal{P}_h(u^n)} \right), \end{aligned} \quad (4.2)$$

or equivalently

$$u^{n+1} = [I - \Delta t^n (A_{\mathcal{D}}^n + \lambda^n I)] u^n + \lambda^n \Delta t^n u_0, \quad (4.3)$$

where the subscript h indicates spatial approximations, for which we will consider difference schemes in the following.

4.1. Spatial schemes for $\mathcal{D} = \Pi_\zeta$. Let (ij) and \mathbf{x}_{ij} denote the (ij) th pixel in the image and $g_{ij} = g(\mathbf{x}_{ij}, \cdot)$. We will drop the superscript n for a simpler presentation. Then, a central finite difference scheme for the x -directional diffusion operator can

be formulated as

$$\begin{aligned}
 \left(\frac{u_{xx}}{\mathcal{P}(u)}\right)_{xx}(\mathbf{x}_{ij}) &\approx \left(\frac{u_{xx}}{\mathcal{P}(u)}\right)_{i-1,j} - 2\left(\frac{u_{xx}}{\mathcal{P}(u)}\right)_{i,j} + \left(\frac{u_{xx}}{\mathcal{P}(u)}\right)_{i+1,j} \\
 &\approx \frac{1}{\mathcal{P}(u)_{i-1,j}}(u_{i-2,j} - 2u_{i-1,j} + u_{i,j}) \\
 &\quad - \frac{2}{\mathcal{P}(u)_{i,j}}(u_{i-1,j} - 2u_{i,j} + u_{i+1,j}) \\
 &\quad + \frac{1}{\mathcal{P}(u)_{i+1,j}}(u_{i,j} - 2u_{i+1,j} + u_{i+2,j}) \\
 &= \frac{1}{\mathcal{P}(u)_{i-1,j}}u_{i-2,j} - \left(\frac{2}{\mathcal{P}(u)_{i-1,j}} + \frac{2}{\mathcal{P}(u)_{i,j}}\right)u_{i-1,j} \\
 &\quad + \left(\frac{1}{\mathcal{P}(u)_{i-1,j}} + \frac{4}{\mathcal{P}(u)_{i,j}} + \frac{1}{\mathcal{P}(u)_{i+1,j}}\right)u_{i,j} \\
 &\quad - \left(\frac{2}{\mathcal{P}(u)_{i,j}} + \frac{2}{\mathcal{P}(u)_{i+1,j}}\right)u_{i+1,j} + \frac{1}{\mathcal{P}(u)_{i+1,j}}u_{i+2,j},
 \end{aligned} \tag{4.4}$$

where

$$\mathcal{P}(u)_{ij} = \frac{|\mathcal{D}_h u_{ij}|}{\rho'(|\mathcal{D}_h u_{ij}|)}.$$

For the boundary condition, we will simply consider the flat extension of the boundary pixel values in the outer normal direction.

The y -directional diffusion operator can be approximated *analogously*:

$$\begin{aligned}
 \left(\frac{u_{yy}}{\mathcal{P}(u)}\right)_{yy}(\mathbf{x}_{ij}) &\approx \frac{1}{\mathcal{P}(u)_{i,j-1}}u_{i,j-2} - \left(\frac{2}{\mathcal{P}(u)_{i,j-1}} + \frac{2}{\mathcal{P}(u)_{i,j}}\right)u_{i,j-1} \\
 &\quad + \left(\frac{1}{\mathcal{P}(u)_{i,j-1}} + \frac{4}{\mathcal{P}(u)_{i,j}} + \frac{1}{\mathcal{P}(u)_{i,j+1}}\right)u_{i,j} \\
 &\quad - \left(\frac{2}{\mathcal{P}(u)_{i,j}} + \frac{2}{\mathcal{P}(u)_{i,j+1}}\right)u_{i,j+1} + \frac{1}{\mathcal{P}(u)_{i,j+2}}u_{i,j+2}.
 \end{aligned} \tag{4.5}$$

The mixed-derivative can be approximated as

$$(u_{xy})_{ij} \approx Q_h u_{ij} := \frac{u_{i+1,j+1} + u_{i-1,j-1} - u_{i-1,j+1} - u_{i+1,j-1}}{4}. \tag{4.6}$$

Note that the approximation of u_{xy} is the same as that of u_{yx} . Thus, we have

$$\left(\frac{u_{xy}}{\mathcal{P}(u)}\right)_{yx}(\mathbf{x}_{ij}) \approx Q_h \left(\frac{Q_h u}{\mathcal{P}_h(u)}\right)_{ij} \approx \left(\frac{u_{yx}}{\mathcal{P}(u)}\right)_{xy}(\mathbf{x}_{ij}). \tag{4.7}$$

4.2. Spatial schemes for $\mathcal{D} = \Delta$. Define the discrete Laplacian Δ_h as

$$\Delta_h u_{ij} = u_{i-1,j} + u_{i+1,j} + u_{i,j-1} + u_{i,j+1} - 4u_{ij}. \tag{4.8}$$

Let

$$R_{ij} = \frac{\Delta_h u_{ij}}{\mathcal{P}(u)_{ij}}, \quad \mathcal{P}(u)_{ij} = \frac{|\Delta_h u_{ij}|}{\rho'(|\Delta_h u_{ij}|)}. \tag{4.9}$$

Then, the diffusion operator can be discretized as

$$\Delta \left(\frac{\Delta u}{\mathcal{P}(u)}\right)(\mathbf{x}_{ij}) \approx \Delta_h R_{ij}, \tag{4.10}$$

which is a difference scheme of 13-point stencil.

4.3. A variable constraint parameter $\{\lambda_{ij}^n\}$. Now, we will present a strategy for λ which is variable. Multiply the stationary part of (4.1) by $(u_0 - u)$ and average the resulting equation *locally* to obtain

$$\lambda(\mathbf{x})\sigma_{\mathbf{x}}^2 \approx \frac{1}{|\Omega_{\mathbf{x}}|} \int_{\Omega_{\mathbf{x}}} (u_0 - u) \mathcal{D} \cdot \left(\frac{\mathcal{D}u}{\mathcal{P}(u)} \right) d\mathbf{x}, \quad (4.11)$$

where $\Omega_{\mathbf{x}}$ is a neighborhood of \mathbf{x} (e.g., the window of (3×3) pixels centered at \mathbf{x}) and $\sigma_{\mathbf{x}}^2$ denotes the local noise variance measured over $\Omega_{\mathbf{x}}$. Then, the right side of the above equation can be approximated, in the n th time level, as in

$$\lambda^n(\mathbf{x}) \approx \frac{1}{\tilde{\sigma}_{\mathbf{x}}^2} \|u_0 - u^n\|_{\mathbf{x}} \|A_{\mathcal{D}}^n u^n\|_{\mathbf{x}}, \quad (4.12)$$

where $A_{\mathcal{D}}^n u^n$ is defined as in (4.2) and $\|g\|_{\mathbf{x}}$ denotes a local average of $|g|$ over $\Omega_{\mathbf{x}}$.

Notice that the constraint parameter in (4.12) is proportional to both the absolute residual $|u_0 - u^n|$ and the diffusion magnitude $|A_{\mathcal{D}}^n u^n|$, which can effectively suppress undesired dissipation that may arise on fast transitions. It also should be noticed that the approximation (4.12) of (4.11) is based on the assumption that $|u_0 - u^n|$ and $|A_{\mathcal{D}}^n u^n|$ are relatively independent, although they may not be. In practice, one can find an effective constraint parameter as follows:

$$\lambda_{ij}^n = \frac{\beta_1}{\tilde{\sigma}^2} |u_{0,ij} - u_{ij}^n| |A_{\mathcal{D}}^n u_{ij}^n|, \quad (4.13)$$

where $\tilde{\sigma}^2$ denotes an estimation of σ^2 and β_1 is a positive constant ($0 < \beta_1 \leq 1$). In this article, we will set $\tilde{\sigma}^2 = \sigma^2$, the true noise variance, when the fourth-order models are compared with the second-order ones.

4.4. Choice of Δt^n . The explicit scheme for fourth-order PDEs in (4.3) is numerically stable only if the timestep size is sufficiently small. In the literature, the timestep size has often been chosen heuristically. However, for efficiency reasons, it is desirable to set Δt^n as large as possible, provided that the algorithm is stable. We will consider an effective strategy for the selection of the timestep size in this subsection.

Note that some coefficients of neighboring values of u_{ij}^n in the right side of (4.3) are always negative and the coefficient of u_{ij}^n itself is conditionally nonnegative; it is hard to analyze mathematical stability for numerical schemes of fourth-order models. It has been observed that the algorithm occasionally diverges when the timestep size is set so as to make the coefficient of u_{ij}^n nonnegative:

$$\Delta t^n \leq \min_{ij} \frac{1}{A_{\mathcal{D},ij}^n + \lambda_{ij}^n}, \quad (4.14)$$

where $A_{\mathcal{D},ij}^n$ is the coefficient of u_{ij}^n in $A_{\mathcal{D}}^n u^n(\mathbf{x}_{ij})$. Thus we will try to choose the timestep size slightly smaller than the one in (4.14):

$$\Delta t^n = \min_{ij} \frac{\gamma}{A_{\mathcal{D},ij}^n + \lambda_{ij}^n}, \quad 0 < \gamma < 1. \quad (4.15)$$

(It has been verified that when $\gamma \geq 0.6$, the resulting algorithm becomes occasionally unstable. We will set $\gamma = 0.5$ in practice.)

For $\mathcal{D} = \Delta$, the coefficient $A_{\mathcal{D},ij}^n$ of u_{ij}^n in $A_{\mathcal{D}}^n u^n$ can be found as

$$A_{\Delta,ij}^n = \frac{1}{\mathcal{P}(u)_{i-1,j}} + \frac{1}{\mathcal{P}(u)_{i+1,j}} + \frac{1}{\mathcal{P}(u)_{i,j-1}} + \frac{1}{\mathcal{P}(u)_{i,j+1}} + \frac{16}{\mathcal{P}(u)_{i,j}},$$

while $A_{\Pi_\zeta, ij}^n$, $\zeta \geq 0$, reads

$$A_{\Pi_\zeta, ij}^n = \frac{1}{\mathcal{P}(u)_{i-1, j}} + \frac{1}{\mathcal{P}(u)_{i+1, j}} + \frac{1}{\mathcal{P}(u)_{i, j-1}} + \frac{1}{\mathcal{P}(u)_{i, j+1}} + \frac{8}{\mathcal{P}(u)_{i, j}} \\ + \frac{\zeta}{8} \left(\frac{1}{\mathcal{P}(u)_{i+1, j+1}} + \frac{1}{\mathcal{P}(u)_{i-1, j-1}} + \frac{1}{\mathcal{P}(u)_{i-1, j+1}} + \frac{1}{\mathcal{P}(u)_{i+1, j-1}} \right).$$

5. NUMERICAL EXPERIMENTS

In this section, we will verify effectiveness of fourth-order image denoising models considered in previous sections. The computation is carried out on a 3.20 GHz desktop having a Linux operating system. The explicit scheme (4.3) is implemented for 15 different models: combinations of five differential operators (Δ , Σ , Π_0 , $\Pi_{1/4}$, and Π_1) and three modulators (ρ_1 , $\rho_{0.6}$, and ρ_{PM}). The input images are first scaled by $1/255$ to have real values between 0 and 1 and then, after denoising, they are scaled back for the 8-bit display in which the pixel values are integers between 0 and 255. When $\rho = \rho_\alpha$, $0 < \alpha \leq 1$, we have $\mathcal{P}(u) = |\mathcal{D}u|^{2-\alpha}$. To prevent the denominators in (4.4), (4.5), (4.7), and (4.9) from approaching zero, a relaxation parameter ε is incorporated:

$$\mathcal{P}(u) \approx (|\mathcal{D}u|^2 + \varepsilon^2)^{(2-\alpha)/2}, \quad \varepsilon > 0.$$

Many of algorithm parameters are chosen heuristically; we set $\varepsilon = 0.01$, $K = 0.03$ in (2.4), and $\gamma = 0.5$ in (4.15). (When $\gamma = 0.6 \sim 0.9$, the explicit scheme has occasionally diverged.) The restoration quality is measured by the *signal-to-noise ratio* (SNR) and the *peak signal-to-noise ratio* (PSNR), which are defined as

$$\text{SNR} \equiv \frac{\sum_{ij} g_{ij}^2}{\sum_{ij} (g_{ij} - h_{ij})^2}, \quad \text{PSNR} \equiv 10 \log_{10} \left(\frac{\sum_{ij} 255^2}{\sum_{ij} (g_{ij} - h_{ij})^2} \right),$$

where g is the original image, h denotes the compared image, and the unit of PSNR is decibel (dB).

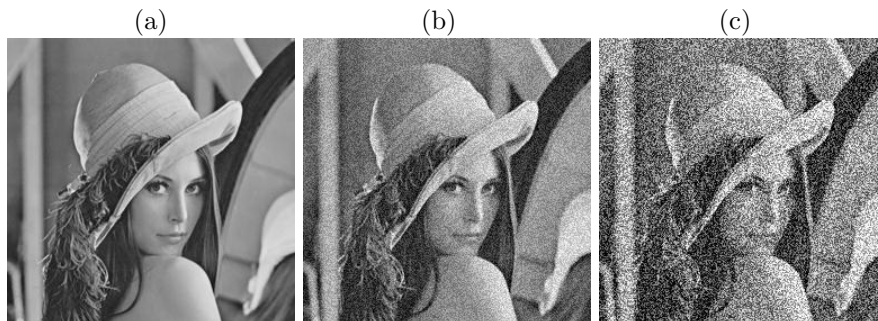


FIGURE 2. Lenna: (a) The original image g and noisy images perturbed by an additive Gaussian noise of (b) PSNR=24.77 (SNR=81.00) and (c) PSNR=15.23 (SNR=9.00).

First, we apply the 15 fourth-order models to the restoration of the Lenna image shown in Figure 2; the noisy images in Figures 2(b) and 2(c) are obtained by perturbing the original image by an additive Gaussian noise of PSNR=24.77 (SNR=81.00) and PSNR=15.23 (SNR=9.00), respectively. We have observed that

it is difficult to set an appropriate stopping criterion for the 15 different models to be compared fairly. Thus the PSNR is computed after each iteration of the explicit scheme (4.3); the models will be compared for the best PSNRs they can achieve for the restored image.

TABLE 1. A PSNR analysis. Set $\beta_1 = 0$ (unconstrained).

PSNR	\mathcal{D}	$\rho = \rho_1$		$\rho = \rho_{0.6}$		$\rho = \rho_{PM}$	
		Iter	PSNR	Iter	PSNR	Iter	PSNR
24.77	Δ	83	30.68	279	30.60	220	30.44
	Σ	40	31.09	104	31.46	119	31.40
	Π_0	46	31.08	129	31.49	78	31.45
	$\Pi_{1/4}$	36	31.21	87	31.63	61	31.52
	Π_1	28	31.07	71	31.44	50	31.34
15.23	Δ	502	25.45	2015	25.48	2492	25.39
	Σ	205	25.58	526	26.01	802	26.05
	Π_0	239	25.59	617	26.06	533	26.05
	$\Pi_{1/4}$	151	25.62	434	26.07	336	25.90
	Π_1	111	25.51	350	25.89	289	25.61

Table 1 shows the best PSNRs and the corresponding iteration counts for the 15 models with no constraint term ($\beta_1 = 0$). For the unconstrained problem, the model with $\mathcal{D} = \Pi_{1/4}$ and $\rho = \rho_{0.6}$ has performed the best in PSNR, for both noise levels. The lowest PSNRs are observed for the models incorporating $\mathcal{D} = \Delta$. Note that the models incorporating $\mathcal{D} = \Pi_1$ have performed not better than the models having $\mathcal{D} = \Pi_0$ (and $\mathcal{D} = \Pi_{1/4}$). When $\mathcal{D} = \Pi_1$, the involvement of cross derivatives into the models is too strong. In order for a non-convex model to hold the PPCs, the model should incorporate $\mathcal{D} = \Pi_\zeta$, $\zeta > 0$; however, ζ should not be too large for an effective denoising. (The models work reasonably well when $\zeta = 0.1 \sim 0.35$.) As one can see from the table (and also from constrained problems in Tables 2 and 3), the models with $\mathcal{D} = \Pi_\zeta$ converge faster, as ζ approaches 1. Such a faster convergence of Π_1 seems due to a *balanced* incorporation of cross derivatives, which in turn makes the finite difference scheme involve a larger number of pixels in various directions in a balanced fashion. For all differential operators (\mathcal{D}), the non-convex models ($\rho = \rho_{0.6}$ and $\rho = \rho_{PM}$) have outperformed over the convex models ($\rho = \rho_1$).

In Table 2, we experiment the same as in Table 1 except for $\beta_1 = 0.4$ in (4.13). For the constrained model, we have observed similar performances as in the unconstrained one. Here the PSNRs are slightly higher, and the PSNR differences between non-convex models and convex ones are smaller than those for the unconstrained models in Table 1. For the high noise level, the constrained model with $\mathcal{D} = \Sigma$ and $\rho = \rho_{0.6}$ has performed the best in PSNR.

In Figure 3, we present the best restored images (measured in PSNR) from the ITV model (2.5) and the fourth-order models, for the high noise level. For the ITV model, the diffusion term is approximated as in [9] and the constraint parameter is set analogously as in Section 4.3; we select a spatially variable timestep size defined as

$$\Delta t_{ij}^n = \frac{\gamma}{A_{ITV,ij}^n + \lambda_{ij}^n}, \quad (5.1)$$

TABLE 2. A PSNR analysis. Set $\beta_1 = 0.4$ (constrained).

PSNR	\mathcal{D}	$\rho = \rho_1$		$\rho = \rho_{0.6}$		$\rho = \rho_{PM}$	
		Iter	PSNR	Iter	PSNR	Iter	PSNR
24.77	Δ	113	30.96	347	30.80	265	30.62
	Σ	59	31.52	137	31.81	147	31.69
	Π_0	65	31.45	166	31.78	97	31.74
	$\Pi_{1/4}$	50	31.53	111	31.90	76	31.83
	Π_1	38	31.38	91	31.73	63	31.67
15.23	Δ	944	26.75	3273	26.55	3709	26.34
	Σ	477	27.32	969	27.44	1200	27.21
	Π_0	521	27.22	1052	27.37	813	27.25
	$\Pi_{1/4}$	331	27.25	745	27.41	514	27.26
	Π_1	251	27.13	619	27.25	475	27.05



FIGURE 3. Lenna: Restored images (best in PSNR) by (a) the ITV model and (b) a fourth-order model, that shows PSNR=26.88 (SNR=131.51, CPU time=0.28 seconds) and PSNR=27.44 (SNR=149.63, CPU time=42.88 seconds), respectively.

where $A_{ITV,ij}^n$ is the coefficient of u_{ij}^n in the approximation of the diffusion term of the ITV model, which is 4 independently on u^n ; see [9] for details. The ITV model shows its best PSNR (=26.88) in 30 iterations, while the fourth-order model with $\mathcal{D} = \Sigma$ and $\rho = \rho_{0.6}$ requires 969 iterations to reach its best PSNR (=27.44). (When the fourth-order models employ the variable timestep size in (5.1), they converge 2-3 times faster, but their best PSNRs are often lowered by an observable amount; fourth-order models have shown higher sensitivity to numerical schemes and parameter choices.) As one can see from the figure, the fourth-order model restores texture regions better than the second-order model, while edges of relatively big contrasts are preserved more clearly by the ITV model. Thus, for untextured images, the second-order model may restore better images than the fourth-order models. The second-order model converges fast without sacrificing the restoration

quality, when the variable timestep size (5.1) is employed. Also, for the second-order model, it is relatively easy to set an appropriate stopping criterion. However, all the fourth-order models except involving $\mathcal{D} = \Delta$ have restored better images than the second-order model.

Another example is given in order to verify the effectiveness of fourth-order models on textured images. We first perturb the original Texture image (Figure 4(a)) by an additive Gaussian noise of PSNR=15.24 (SNR=11.51); see Figure 4(b).

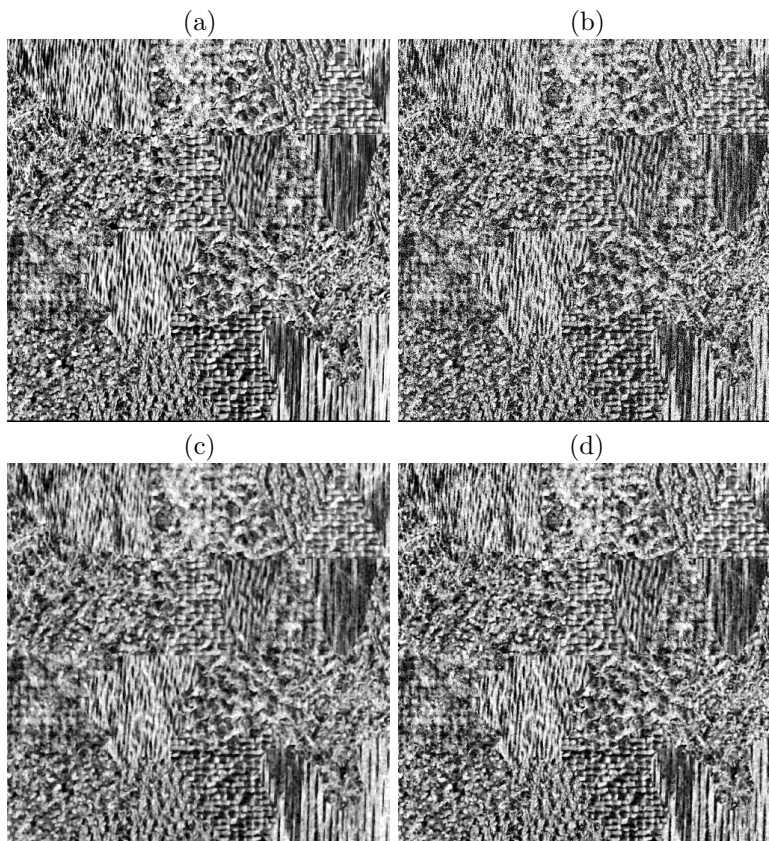


FIGURE 4. Texture: (a) The original image g , (b) noisy image perturbed by an additive Gaussian noise of PSNR=15.24 (SNR=11.51), and the restored images by (c) the ITV model, PSNR=18.21 (SNR=22.80) and (d) the fourth-order model, PSNR=19.22 (SNR=28.78).

Figure 4(c) represents recovered image using the ITV model with the spatially variable timestep size (5.1) and Figure 4(d) is a denoised image using the fourth-order model ($\mathcal{D} = \Pi_{1/4}$ and $\rho = \rho_{0.6}$). After results are measured in PSNR and visual verification, the ITV model shows its best recovered image after only 3 iterations (PSNR= 18.21, CPU time=0.33 seconds). The fourth-order model reaches its best PSNR (=19.22) after 353 iterations (CPU time=65.05 seconds). As one can see from the figures, the fourth-order model preserves textures better than the ITV

model. Although ITV model gives the results faster than the fourth-order model, the difference is not significant.



FIGURE 5. Test images: (a) Bamboo, (b) Elaine, and (c) Poker Chips.

We select a set of images as in Figure 5, for more tests and comparisons.

Table 3 presents a PSNR analysis, showing the best PSNRs and the corresponding iteration counts, for the 15 different constrained fourth-order models applied to the restoration of three images in Figure 5. As one can see from the table, we have again reached the same conclusions: (a) the models incorporating $\mathcal{D} = \Pi_1$ converge fastest and (b) non-convex models outperform over convex models. When the ITV model (2.5) is applied, the best PSNRs turn out to be 32.44, 28.10, and 24.68 respectively for Bamboo, Elaine, and Poker Chips; the fourth-order models holding the PPCs restore better images than the second-order model for all cases.

TABLE 3. A PSNR analysis. Set $\beta_1 = 0.4$ (constrained).

Image (PSNR)	\mathcal{D}	$\rho = \rho_1$		$\rho = \rho_{0.6}$		$\rho = \rho_{PM}$	
		Iter	PSNR	Iter	PSNR	Iter	PSNR
Bamboo (16.81)	Δ	1186	32.04	3597	31.71	3326	31.34
	Σ	778	32.66	1251	32.82	1126	32.32
	Π_0	724	32.45	1186	32.60	787	32.33
	$\Pi_{1/4}$	523	32.86	844	33.14	534	32.82
	Π_1	406	33.29	678	33.56	491	33.29
Elaine (16.81)	Δ	802	28.06	2627	27.85	2706	27.58
	Σ	416	28.46	748	28.54	912	28.48
	Π_0	414	28.43	864	28.56	602	28.51
	$\Pi_{1/4}$	282	28.45	570	28.59	407	28.50
	Π_1	219	28.32	468	28.43	371	28.30
Poker Chips (16.82)	Δ	383	24.59	1581	24.57	1965	24.45
	Σ	184	25.15	491	25.55	776	25.44
	Π_0	194	24.97	565	25.44	501	25.48
	$\Pi_{1/4}$	144	25.16	418	25.66	319	25.64
	Π_1	110	25.19	361	25.61	276	25.54

Figure 6 depicts a noisy image of Elaine and restored images by two constrained fourth-order models: $\mathcal{D} = \Delta$ and $\mathcal{D} = \Pi_{1/4}$. For both models, we set $\rho = \rho_{0.6}$

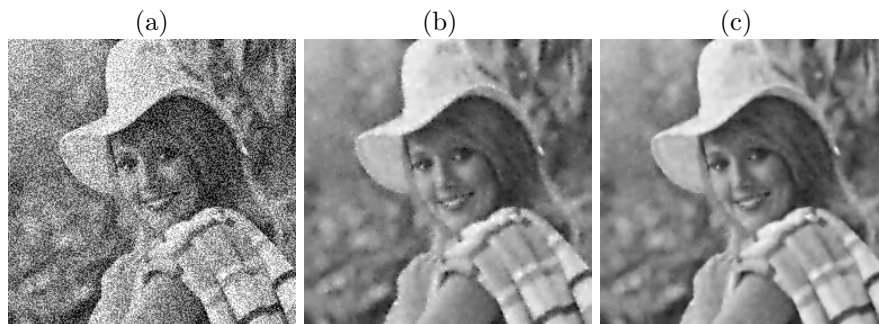


FIGURE 6. Elaine: (a) A noisy image of PSNR=16.82 (SNR=15.29) and restored images by (b) $\mathcal{D} = \Delta$ and (c) $\mathcal{D} = \Pi_{1/4}$. For both models, we set $\rho = \rho_{0.6}$ and $\beta_1 = 0.4$.

and $\beta_1 = 0.4$. The restored image with $\mathcal{D} = \Delta$ incorporates speckles, which is objectionable, as in Figure 6(b). On the other hand, the model of $\mathcal{D} = \Pi_{1/4}$ has restored edges and fine structures more clearly. It is apparent that fourth-order models holding the PPCs can suppress speckles effectively and result in better images than models without PPCs.

CONCLUSIONS

Properties of a variational model in image denoising are combined effects of the differential operator, the modulator, and the constraint term. In this article, we have introduced *piecewise planarity conditions* (PPCs) for fourth-order variational denoising models in continuum. For an efficient simulation of fourth-order variational models, we have considered effective numerical methods such as a variable constraint parameter and a stable timestep size. Although the PPCs may not be satisfied by discrete data (images) in the same way as in continuum, they may serve as a valuable mathematical tool for the advancement of the state-of-the-art methods for PDE-based denoising. Models with the PPCs have proved to be able to restore better images measured in PSNR (and visual inspection) than models without PPCs. Also, it has been observed that fourth-order variational models can restore better images than second-order ones, particularly when they hold the PPCs. Fourth-order models have restored texture regions favorably, while second-order models tend to restore edges of large contrasts more clearly.

Acknowledgment. The work of the author is supported in part by NSF grants DMS-0630798 and DMS-0609815. The code utilized for this article has been implemented for the modelcode library: *Graduate Research and Applications for Differential Equations* (GRADE), and is available at www.msstate.edu/~skim/GRADE or by asking the author via email (skim@math.msstate.edu).

REFERENCES

- [1] L. Alvarez, P. Lions, and M. Morel; Image selective smoothing and edge detection by nonlinear diffusion. II, *SIAM J. Numer. Anal.*, vol. 29, pp. 845–866, 1992.
- [2] S. Angenent, E. Pichon, and A. Tannenbaum; Mathematical methods in medical image processing, *Bulletin of the American Mathematical Society*, vol. 43, no. 3, pp. 365–396, 2006.

- [3] F. Catte, P. Lions, M. Morel, and T. Coll; Image selective smoothing and edge detection by nonlinear diffusion. *SIAM J. Numer. Anal.*, vol. 29, pp. 182–193, 1992.
- [4] T. Chan, S. Osher, and J. Shen; The digital TV filter and nonlinear denoising, Department of Mathematics, University of California, Los Angeles, CA 90095-1555, Technical Report #99-34, October 1999.
- [5] T. Chan and J. Shen; *Image Processing and Analysis*. Philadelphia: SIAM, 2005.
- [6] J. Douglas, Jr. and J. Gunn; A general formulation of alternating direction methods Part I. Parabolic and hyperbolic problems, *Numer. Math.*, vol. 6, pp. 428–453, 1964.
- [7] J. Douglas, Jr. and S. Kim; Improved accuracy for locally one-dimensional methods for parabolic equations, *Mathematical Models and Methods in Applied Sciences*, vol. 11, pp. 1563–1579, 2001.
- [8] S. Kim; PDE-based image restoration: A hybrid model and color image denoising, *IEEE Trans. Image Processing*, vol. 15, no. 5, pp. 1163–1170, 2006.
- [9] S. Kim and H. Lim; A non-convex diffusion model for simultaneous image denoising and edge enhancement, *Electronic Journal of Differential Equations*, Conference 15, pp. 175–192, 2007.
- [10] M. Lysaker, A. Lundervold, and X.-C. Tai; Noise removal using fourth-order partial differential equation with applications to medical magnetic resonance images in space and time, *IEEE Trans. Image Process.*, vol. 12, no. 12, pp. 1579–1590, 2003.
- [11] A. Marquina and S. Osher; Explicit algorithms for a new time dependent model based on level set motion for nonlinear deblurring and noise removal, *SIAM J. Sci. Comput.*, vol. 22, pp. 387–405, 2000.
- [12] Y. Meyer; *Oscillating Patterns in Image Processing and Nonlinear Evolution Equations*, ser. University Lecture Series. Providence, Rhode Island: American Mathematical Society, 2001, vol. 22.
- [13] M. Nitzberg and T. Shiota; Nonlinear image filtering with edge and corner enhancement, *IEEE Trans. on Pattern Anal. Mach. Intell.*, vol. 14, pp. 826–833, 1992.
- [14] S. Osher, M. Burger, D. Goldfarb, J. Xu, and W. Yin; Using geometry and iterated refinement for inverse problems (1): Total variation based image restoration, Department of Mathematics, UCLA, LA, CA 90095, CAM Report #04-13, 2004.
- [15] S. Osher and R. Fedkiw; *Level Set Methods and Dynamic Implicit Surfaces*. New York: Springer-Verlag, 2003.
- [16] S. Osher, A. Solé, and L. Vese; Image decomposition and restoration using total variation minimization and the H^{-1} norm,” *SIAM J. Multiscale Model. Simul.*, vol. 1, no. 3, pp. 349–370, 2003.
- [17] P. Perona and J. Malik; Scale-space and edge detection using anisotropic diffusion, *IEEE Trans. on Pattern Anal. Mach. Intell.*, vol. 12, pp. 629–639, 1990.
- [18] L. Rudin, S. Osher, and E. Fatemi; Nonlinear total variation based noise removal algorithms, *Physica D*, vol. 60, pp. 259–268, 1992.
- [19] R. Weinstock; *Calculus of Variations*. New York: Dover Publications, Inc., 1974.
- [20] Y.-L. You and M. Kaveh; Fourth-order partial differential equations for noise removal, *IEEE Trans. Image Process.*, vol. 9, pp. 1723–1730, 2000.
- [21] Y.-L. You, W. Xu, A. Tannenbaum, and M. Kaveh; Behavioral analysis of anisotropic diffusion in image processing, *IEEE Trans. Image Process.*, vol. 5, pp. 1539–1553, 1996.

SEONGJAI KIM

DEPARTMENT OF MATHEMATICS & STATISTICS, MISSISSIPPI STATE UNIVERSITY, MISSISSIPPI STATE, MS 39762, USA

E-mail address: skim@math.msstate.edu

HYEONA LIM

DEPARTMENT OF MATHEMATICS & STATISTICS, MISSISSIPPI STATE UNIVERSITY, MISSISSIPPI STATE, MS 39762, USA

E-mail address: hlim@math.msstate.edu